ChemComm
Chemical Communications

Accepted Manuscript

This article can be cited before page numbers have been issued, to do this please use: Y. Li, T. Toriyama, T. Yamamoto, Y. Murakami, H. Ashitani, S. Kawaguchi, Y. Kubota, H. Kitagawa and K. Kusada, *Chem. Commun.*, 2026, DOI: 10.1039/D5CC06643C.

ROYAL SOCIETY OF CHEMISTRY

rsc.li/chemcomm

ChemComm

View Article Online
DOI: 10.1039/D5CC06643C

COMMUNICATION

Rapid synthesis of $SrRuO_3$ using supercritical water fluid with improved oxygen evolution activity

Received 00th January 20xx,
Accepted 00th January 20xx

DOI: 10.1039/x0xx00000x

Yumeng Li,[a] Takaaki Toriyama,[b] Tomokazu Yamamoto,[b] Yasukazu Murakami,[bc] Hirotaka Ashitani,[d] Shogo Kawaguchi,[d] Yoshiki Kubota,[e] Hiroshi Kitagawa,[a*] and Kohei Kusada[afgh*]

Perovskite oxides are typically synthesised using hydrothermal and sol–gel methods, which require long reaction times and can result in broadened nucleation. Herein, we report a rapid, one-step facile synthesis of $SrRuO_3$ using supercritical water fluid that offers improved oxygen evolution reaction activity compared with the conventional batch hydrothermal method.

The development of rapid, controllable, and scalable synthesis routes for metal oxides remains challenging in materials chemistry. Conventional sol–gel and hydrothermal methods typically require hours to days at elevated temperatures and sometimes harsh alkaline conditions.[1-3] Hydrothermal batch synthesis, in particular, exhibits broadened nucleation and growth owing to long heat-up and cool-down times.[4] Moreover, post-synthetic calcination is typically required for both methods to improve crystallinity.[2,3]

Supercritical-water-flow synthesis provides a fundamentally different synthesis method. When water is heated above its critical point (374 °C, 22.1 MPa), its dielectric constant decreases, whereas its diffusivity and ionic product increase. This results in an exceptionally reactive medium.[4–6] In a continuous-flow reactor, cold precursor solutions combine rapidly with supercritical water, while the abrupt change in solvent properties promotes near-instantaneous supersaturation, nucleation, and crystallisation within a residence time of only a few seconds.[4,7,8] While other rapid synthesis approaches such as microwave-assisted and solution-combustion methods can reduce reaction times to the order of minutes or seconds, they often encounter issues such as non-uniform heating and difficulty in controlling reaction temperature.[9,10] In contrast, supercritical-flow offers precise temperature and mixing control through the flow rate and reactor geometry, thus ensuring reproducibility and scalability.[4,11,12] Additionally, its continuous operation enables a straightforward scaling up by merely increasing the amount of the precursor solution. Beyond speed and scalability, the non-equilibrium reaction conditions of this process impart qualities that are not typically accessible in slow, conventional syntheses. Supercritical flow can yield materials with subtle structural or chemical features that differ from those synthesised through gradual thermal growth, including possible variations in oxidation state and oxygen content.[4] These non-equilibrium effects of supercritical water highlight that this method not only crystallises oxides rapidly but also enables access to metastable states and structures that can offer functional advantages.

Supercritical-water-flow synthesis is a promising method for synthesising perovskite oxides, whose flexible framework readily accommodates diverse cation combinations and oxygen stoichiometries.[13] Among their many applications (e.g. electrocatalysis and spintronics), we focus on oxygen evolution reaction (OER) catalysis, i.e. the rate-limiting step in water electrolysis,[14] where the tunable electronic structure and oxygen vacancy of perovskites are relevant.[15] As a model system, we selected strontium ruthenate ($SrRuO_3$) owing to its relatively high theoretically predicted OER activeness and structural flexibility,[16,17] which render it a natural platform for investigating possible differences in electronic structure and electrochemical performance between supercritical conditions with rapid crystallisation and the conventional batch-hydrothermal synthesis. Additionally, $SrRuO_3$

[a] Division of Chemistry, Graduate School of Science, Kyoto University, Kyoto 606-8502, Japan. Email: kitagawa@kuchem.kyoto-u.ac.jp
[b] The Ultramicroscopy Research Center, Kyushu University, Fukuoka 819-0395, Japan
[c] Department of Applied Quantum Physics and Nuclear Engineering, Graduate School of Engineering, Kyushu University, 744 Motooka, Nishi-ku, Fukuoka 819-0395, Japan
[d] Japan Synchrotron Radiation Research Institute (JASRI), Hyogo 679-5198, Japan
[e] Department of Physics, Graduate School of Science, Osaka Metropolitan University, Osaka 558-8585, Japan
[f] The HAKUBI Center for Advanced Research, Kyoto University, Kyoto 606-8502, Japan
[g] Institute of Advanced Study, Kyushu University, Fukuoka 816-8580, Japan
[h] Faculty of Engineering Sciences, Kyushu University, Fukuoka 816-8580, Japan. Email: kusada.kohei.236@m.kyushu-u.ac.jp

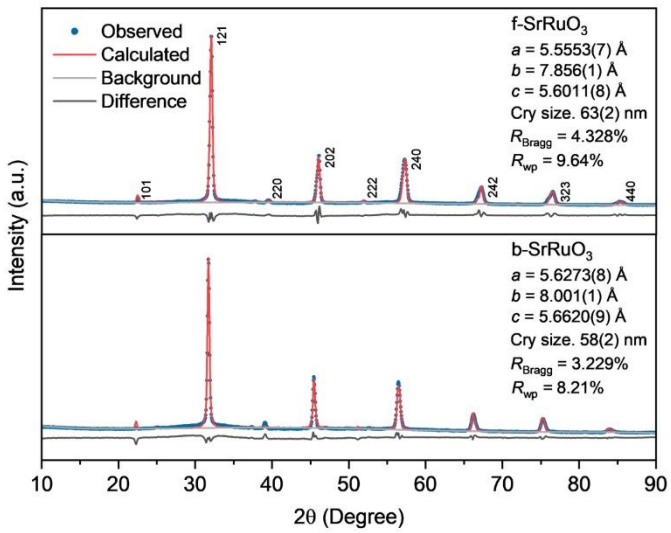

Figure 1. XRD patterns and fitting results by Rietveld refinement of f-$SrRuO_3$ and b-$SrRuO_3$ (λ = 1.54 Å).

cannot be easily synthesised via the hydrothermal method and reports regarding its batch synthesis are scarce. Herein, we report the first successful synthesis of crystalline $SrRuO_3$ under supercritical water flow, which yielded nanocrystals with distinct OER activity compared with batch-hydrothermal analogues.

$SrRuO_3$ was synthesised via both the supercritical-water-flow (f-$SrRuO_3$) and batch-hydrothermal (b-$SrRuO_3$) methods. For the flow synthesis, 50 mL of a metal precursor solution was prepared by dissolving 0.42 mmol each of $RuCl_3{\cdot}xH_2O$ and $Sr(NO_3)_2$ in deionised water, while another 50 mL of 0.3 M NaOH solution was prepared separately. During the operation of the flow reactor, deionised water was pumped at a rate of 80 mL/min, pressurised to 25 MPa, and heated to 376 °C to generate supercritical water. The precursor and NaOH solutions were fed into the reactor at a rate of 5 mL/min and mixed with the supercritical stream (Fig. S1). Nucleation and crystallisation occurred during the flow from the mixer to the chiller prior to being quenched in the chiller. The resulting suspension was collected and then the precipitates were separated via centrifugation and washed with deionised water. Subsequently, they were vacuum dried and then treated with 0.02 M HCl to remove impurities, followed by rewashing with deionised water and vacuum drying to obtain f-$SrRuO_3$. For batch-hydrothermal synthesis, 0.42 mmol of each of $KRuO_4$ and $Sr(NO_3)_2$ were dissolved in 50 mL of saturated NaOH solution and sealed in a Teflon-lined autoclave. Subsequently, the mixture was heated to 175 °C at 2 °C/min and reacted for 24 h. The product was collected, washed with deionised water, and vacuum dried to obtain b-$SrRuO_3$. Typical average yield for supercritical flow synthesis is 13 mg before HCl washing and 3 mg after washing, while the typical average yield is 6 mg for batch synthesis.

The phase purity and crystallographic structure of the as-synthesised samples were verified via powder X-ray diffraction (XRD). XRD provided direct evidence of the crystal structure as well as quantitative lattice parameters using Rietveld refinement. The diffraction patterns of both f-$SrRuO_3$ and b-$SrRuO_3$ were indexed to the orthorhombic perovskite structure of $SrRuO_3$ (COD #96-153-

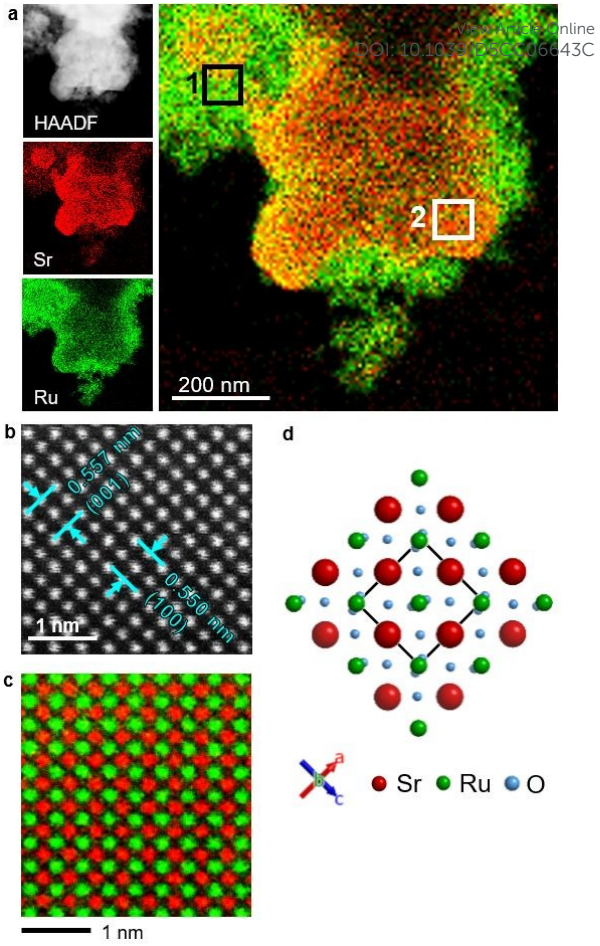

Figure 2. (a) HAADF and STEM-EDX maps of Sr-L (red) and Ru-L (green) showing Ru-rich region (region 1) and regions with Sr and Ru evenly distributed (region 2), atomic-resolution (b) HAADF image and (c) EDX map, and (d) structural model of $SrRuO_3$ viewed along the [010] direction.

3614), as shown in Fig. S2, thus indicating that both have adopted the expected perovskite phase while TEM images in Fig. S3 shows the agglomerated particles. Rietveld refinement of the obtained patterns (Fig. 1) further revealed subtle lattice distortions. Compared with the values reported for bulk $SrRuO_3$ (*a* = 5.5684 Å, *b* =7.8452 Å, and *c* = 5.5320 Å),[18] f-$SrRuO_3$ showed a slight contraction in the length of *a* axis and increase in length of *b* and *c* axis while, b-$SrRuO_3$ exhibited larger length values in all three *a*, *b* and *c* axes. Such anisotropic changes may have been induced by the different synthesis methods used (calcination and sintering in Bansal et al.'s study[18] vs. batch hydrothermal and flow synthesis without calcination in our study). To complement these bulk structural results, the microstructure and elemental distribution were examined using scanning transmission electron microscopy (STEM) coupled with energy-dispersive X-ray spectroscopy (STEM-EDX). Elemental maps of Sr and Ru show that both f-$SrRuO_3$ and b-$SrRuO_3$ (Figs. 2a and S4) contain two distinguishable regions: a uniform crystalline region containing both Sr and Ru, which corresponds to $SrRuO_3$, and a Ru-rich amorphous region. The Ru-rich region is attributed to a minor impurity phase, which may partially originate from non-stoichiometric (hydro)oxides,

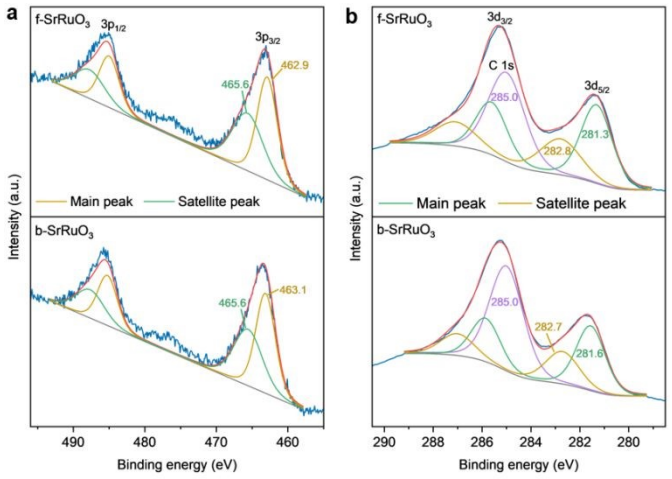

Figure 3. XPS spectra for f-$SrRuO_3$ and b-$SrRuO_3$. (a) Ru 3p and (b) Ru 3d.

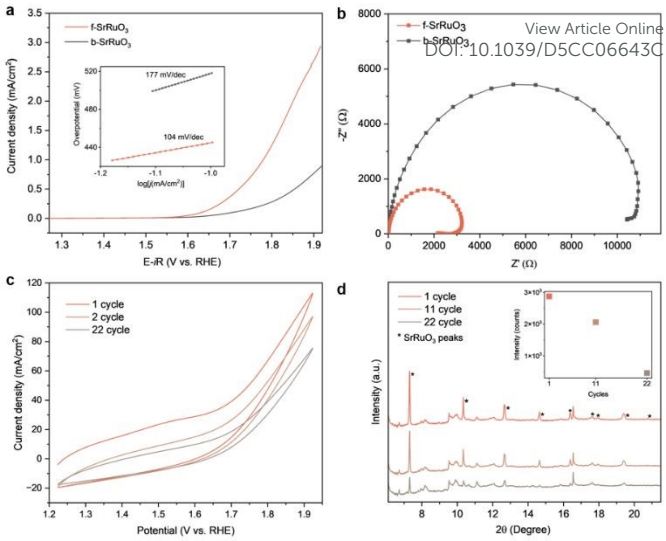

Figure 4.CV cycling stability test for h-$SrRuO_3$ and f-$SrRuO_3$. (a) LSV and (b) EIS. Operando measurement results with (c) CV cycling and (d) XRD measurements obtained simultaneously (λ = 0.35 Å) with inset showing the intensity of the main peak (at approximately 2ϑ = 7.3°) as a function of cycle number.

as it contains both Sr and Ru (Table S1). Atomic-resolution high-angle annular dark-field (HAADF) STEM imaging and EDX mapping of f-$SrRuO_3$ (Figs. 2b and 2c) provided confirmation at the atomic scale of the perovskite arrangement. The image showed the expected sublattices composed of Sr and Ru, respectively and is consistent with the ideal $SrRuO_3$ structure viewed along the [010] direction (Fig. 2d). For the crystalline region, the lattice spacings of the (001) and (100) planes (0.557 and 0.550 nm, respectively) were extracted from the HAADF image in Fig. 2b, and the values were in good agreement with those obtained from Rietveld refinement. This indicates that the local structure imaged via HAADF is consistent with the long-range atomic order confirmed by Rietveld refinement, thus confirming the formation of a well-ordered perovskite lattice, even within the sub-second crystallisation timeframe of the supercritical-flow synthesis.

To analyse the electronic states of Sr and Ru, X-ray photoelectron spectroscopy (XPS) was performed for b-$SrRuO_3$ and f-$SrRuO_3$ and the XPS spectra were calibrated by setting the C 1s peak at 285.0 eV.[19] The Sr 3d XPS result (Fig. S5) showed that both samples were in the Sr^{2+} state with peak positions (Table S2) similar to previously reported values of 132.2-133.7 eV.[20] In the Ru 3p spectra for b-$SrRuO_3$ and f-$SrRuO_3$, the peak position of $3p_{3/2}$ for b-$SrRuO_3$ at 463.3 eV was similar to the previously reported value of the main peak, i.e. approximately 463.2 eV[20,21], and was consistent with the Ru^{4+} oxidation-state characteristic of stoichiometric $SrRuO_3$. However, the peak position for f-$SrRuO_3$ is downshifted by 0.4 eV, thus indicating a slightly reduced state from Ru^{4+}. Measurements of the Ru 3d region reinforced this observation. In the Ru 3d measurement, a slight upshift of 0.3 eV was observed in the $3d_{5/2}$ peak for b-$SrRuO_3$ when compared with the previously reported value of approximately 281.3 eV[22,23], whereas f-$SrRuO_3$ has a similar value. However, when the peak positions of f-$SrRuO_3$ and b-$SrRuO_3$ were compared, a downshift in the peak positions of f-$SrRuO_3$ was again observed. This result reaffirms the possibility of partial Ru reduction in f-$SrRuO_3$. One possible reason for this is oxygen deficiency in the perovskite phase. Another possibility for the charge state reduction is the presence of non-stoichiometric (hydro)oxides that might be present in the amorphous region, as observed in STEM, which might favour the partial reduction of Ru from stoichiometric Ru^{4+}.

Having confirmed the structural integrity and oxidation state of f-$SrRuO_3$ and b-$SrRuO_3$, OER measurements were performed on both samples to evaluate whether the rapidly synthesised f-$SrRuO_3$ maintained a similar OER activity to that of b-$SrRuO_3$, which was synthesised via a more conventional route. All measurements were performed in 1 M KOH using a standard three-electrode system (details of the procedure in Supplemental Information). Linear sweep voltammetry (LSV) revealed a pronounced activity enhancement for f-$SrRuO_3$, where it delivered a current density and a mass activity approximately three times higher than that of b-$SrRuO_3$ at the highest measured potential of 1.92 V vs. RHE (Figs. 4a and S8). Additionally, the corresponding Tafel slope of 104 mV/dec was smaller than that of the batch-synthesised sample (177 mV/dec), thus indicating that f-$SrRuO_3$ was more responsive to changes in the applied potential. The electrochemical impedance (EIS) data further support these findings. The plot presented in Fig. 4b shows that f-$SrRuO_3$ possesses a smaller charge-transfer resistance (R_{ct}) (Table S4) than b-$SrRuO_3$. As the surface area used can affect the apparent current density, we further normalised the LSV curves to the electrochemically active surface area (ECSA), which was determined from the double-layer capacitance obtained via cyclic voltammetry (CV) at various scan rates (Fig. S6). As shown in Fig. S7, even after this normalisation, f-$SrRuO_3$ retained a higher current density than that by b-$SrRuO_3$, thus indicating a higher intrinsic activity of the catalytically active sites in f-$SrRuO_3$.This result combined with the larger calculated ECSA for f-$SrRuO_3$ (Table S4) suggests that the enhanced OER current density of f-$SrRuO_3$ arises from a dual contribution: a higher intrinsic activity of the active sites and an

increased density of accessible active sites. One possible contributor to this increase in catalytic activity may be the change in the electronic structure of Ru, which can increase the electrical conductivity and exposure of active sites in perovskite oxides, as previously reported in the literature.[15,24] Specifically, prior studies on Ru-based oxides such as RuO_2 have shown that a reduction in Ru oxidation state can enhance *OOH adsorption and decrease the energy barrier for the rate-determining *O to *OOH step and thereby lower the OER overpotential.[25] The slightly reduced Ru in f-$SrRuO_3$ may have induced analogous electronic effects that promoted *OOH formation, and thus provide a possible explanation for its enhanced OER activity. Another possibility is that the minor impurity phase could have had a positive effect on OER activity. However, as the impurity content is low, the main contributor to the enhanced OER activity is still likely $SrRuO_3$. The durability of the catalysts was investigated via cyclic voltammetry (CV) cycling. Fig. S9 shows that both b-$SrRuO_3$ and f-$SrRuO_3$ exhibited a gradual decrease in current density upon repeated cycling. However, the decline was less pronounced for f-$SrRuO_3$, thus indicating the slightly improved stability of f-$SrRuO_3$ in alkaline OER conditions. To investigate the origin of the activity loss, operando XRD measurement during the CV cycling of f-$SrRuO_3$ was conducted at SPring-8 BL13XU (Fig. S10).[26] The results were consistent with those of the stability test, and the current density decreased progressively with increasing cycling (Fig. 4c). The simultaneously recorded XRD patterns revealed that the characteristic peaks of $SrRuO_3$ decreased steadily and was almost undetectable after 22 cycles, indicating a progressive structural breakdown (Fig. 4d). STEM-EDX map of the post-cycled electrode catalyst (from the stability test) has also provided support of compositional change (Fig. S11). Regions containing only Sr were detected and implies the dissolution of Ru from the perovskite structure. This observation suggests that the decrease in current density is due to Ru dissolution, which is consistent with previous studies linking the limited alkaline stability of $SrRuO_3$ to Ru leaching.[15,27] Some possible strategies to improve $SrRuO_3$ stability would be A- and/or B-site doping. A-site substitution can modify lattice structure, oxygen vacancy content and B-site oxidation states to improve stability[29] while B-site doping directly tune M–O covalency, mitigating a stability limitation of ABO_3 perovskites.[28] Collectively, these approaches could provide a rational basis for stabilizing $SrRuO_3$ under OER conditions.

In summary, we demonstrated the rapid synthesis of $SrRuO_3$ via supercritical-water-flow synthesis with a crystallisation time of less than 1 s and under much milder alkaline conditions compared with those of batch-hydrothermal synthesis. The resulting f-$SrRuO_3$ sample was crystalline with slightly reduced Ru species, as inferred from XPS measurements. Electrochemical measurements further showed that f-$SrRuO_3$ exhibited higher OER activity than the batch-hydrothermal sample. These results indicate that supercritical water flow synthesis is a viable method for preparing perovskite oxides, thus facilitating the synthesis of perovskites customised to different reactions by varying the metal combinations.

Conflicts of interest

There are no conflicts to declare.

View Article Online
DOI: 10.1039/D5CC06643C

Data availability

The data supporting this article have been included as part of the SI.

Acknowledgements

We acknowledge support from JST SPRING grant (number JPMJSP2110), JSPS KAKENHI grant (numbers JP25K01622, JP20H05623, JP25H01669, and 25H00804), JST FOREST JPMJFR221P and the ENEOS Hydrogen Trust Fund. This work was partially supported by the Demonstration Project of Innovative Catalyst Technology for Decarbonization through Regional Resource Recycling, Ministry of the Environment, Government of Japan, and Kyushu University Inamori Frontier Program. Synchrotron XRD measurements were performed at beamline BL13XU in SPring-8 under proposal number 2024B2058. STEM analyses were supported by Advanced Research Infrastructure for Materials and Nanotechnology in Japan (ARIM) of the Ministry of Education, Culture, Sports, Science and Technology (MEXT) (Proposal Numbers JPMXP12225KU0003 and JPMXP12225KU0004).

Notes and references

1 T. Ye, Z. Dong, Y. Zhao, J. Yu, F. Wang, L. Zhang and Y. Zou, *Dalton Trans*., 2011, 40, 2601–2606.
2 X. Xue and B. Li, *Nanomaterials*, 2025, **15**, 472.
3 E. Danks, S. R. Hall and Z. Schnepp, *Mater. Horiz*., 2016, **3**, 91–112.
4 J. A. Darr, J. Zhang, N. M. Makwana and X. Weng, *Chem. Rev*., 2017, **117**, 11125–11238.
5 J. Becker, P. Hald, M. Bremholm, J. S. Pedersen, J. Chevallier, S. B. Iversen and B. B. Iversen, *ACS Nano*, 2008, **2**, 1058–1068.
6 T. Adschiri, Y.-W. Lee, M. Goto and S. Takami, *Green Chem.*, 2011, **13**, 1380–1390.
7 S. Hanabata, K. Kusada, T. Yamamoto, T. Toriyama, S. Matsumura, S. Kawaguchi, Y. Kubota, Y. Nishida, M. Haneda and H. Kitagawa, J. Am. Chem. Soc., 2024, 146, 181–186.
8 Q. Li, L. Liu, Z. Wang and X. Wang, *Nanomaterials*, 2022, 12, 668.
9 T. Sajini and J. Joseph, *RSC Sustainability*, 2025, **3**, 4911–4935.
10 A. Varma, A. S. Mukasyan, A. S. Rogachev and K. V. Manukyan, *Chem. Rev.*, 2016, **116**, 14493–14586.
11 A. A. Chaudhry, S. Haque, S. Kellici, P. Boldrin, I. Rehman, F. A. Khalid and J. A. Darr, *Chem. Comm*., 2006, 2286–2288.
12 D. Malarde, I. D. Johnson, I. J. Godfrey, M. J. Powell, G. Cibin, R. Quesada-Cabrera, J. A. Darr, C. J. Carmalt, G. Sankar, I. P. Parkin and R. G. Palgrave, *J. Mater. Chem. C*, 2018, 6, 11731–11739.
13 L.-B. Liu, C. Yi, H.-C. Mi, S. L. Zhang, X.-Z. Fu, J.-L. Luo and S. Liu, *Electrochem. Energy Rev*., 2024, 7, 14.
14 N.-T. Suen, S.-F. Hung, Q. Quan, N. Zhang, Y.-J. Xu and H. M. Chen, *Chem. Soc. Rev*., 2017, 46, 337–365.
15 J.-W. Zhao, Y. Li, D. Luan and X. W. (David) Lou, *Sci. Adv*., 10, eadq4696.
16 I. C. Man, H.-Y. Su, F. Calle-Vallejo, H. A. Hansen, J. I. Martínez, N. G. Inoglu, J. Kitchin, T. F. Jaramillo, J. K. Nørskov and J. Rossmeisl, *ChemCatChem*, 2011, **3**, 1159–1165.
17 M. Cuoco and A. Di Bernardo, *APL Mater*., 2022, **10**, 090902.
18 C. Bansal, H. Kawanaka, R. Takahashi and Y. Nishihara, *J. Alloys and Compd*., 2003, **360**, 47–53.

View Article Online
DOI: 10.1039/D5CC06643C

19 P. Swift, *Surf. Interface Anal.*, 1982, **4**, 47–51.
20 Q. Li, D. Wang, Q. Lu, T. Meng, M. Yan, L. Fan, Z. Xing and X. Yang, *Small*, 2020, **16**, 1906380.
21 Y. K. Wakabayashi, S. Kaneta-Takada, Y. Krockenberger, K. Takiguchi, S. Ohya, M. Tanaka, Y. Taniyasu and H. Yamamoto, *AIP Adv*., 2021, **11**, 035226.
22 I. Rodríguez-García, D. Galyamin, L. Pascual, P. Ferrer, M. A. Peña, D. Grinter, G. Held, M. Abdel Salam, M. Mokhtar, K. Narasimharao, M. Retuerto and S. Rojas, *J. Power Sources*, 2022, **521**, 230950.
23 S. A. Lee, S. Oh, J.-Y. Hwang, M. Choi, C. Youn, J. W. Kim, S. H. Chang, S. Woo, J.-S. Bae, S. Park, Y.-M. Kim, S. Lee, T. Choi, S. W. Kim and W. S. Choi, *Energy Environ. Sci*., 2017, **10**, 924–930.
24 H. Arandiyan, S. S. Mofarah, Y. Wang, C. Cazorla, D. Jampaiah, M. Garbrecht, K. Wilson, A. F. Lee, C. Zhao and T. Maschmeyer, *Chem. Eur. J.*, 2021, **27**, 14418–14426.
25 C. Zhou, L. Li, Z. Dong, F. Lv, H. Guo, K. Wang, M. Li, Z. Qian, N. Ye, Z. Lin, M. Luo and S. Guo, *Nat. Commun.*, 2024, **15**, 9774.
26 S. Kawaguchi, S. Kobayashi, H. Yamada, H. Ashitani, M. Takemoto, Y. Imai, T. Hatsui, K. Sugimoto and O. Sakata, *J. Synchrotron Rad.*, 2024, **31**, 955–967.
27 S. H. Chang, N. Danilovic, K.-C. Chang, R. Subbaraman, A. P. Paulikas, D. D. Fong, M. J. Highland, P. M. Baldo, V. R. Stamenkovic, J. W. Freeland, J. A. Eastman and N. M. Markovic, *Nat. Commun.*, 2014, **5**, 4191.
28 Y. Liu, H. Huang, L. Xue, J. Sun, X. Wang, P. Xiong and J. Zhu, *Nanoscale*, 2021, **13**, 19840–19856.
29 Xiaorongjiao, Y. Liu, X. Jiang, C. Xing, X. Qi, X. Wang and A. Cabot, *Chem. Eng. J.*, 2025, **525**, 169987.

View Article Online
DOI: 10.1039/D5CC06643C

The data supporting this article have been included as part of the SI.